2

The gravitational lens B1600+434: A precision Time-delay and evidence for continuous Extrinsic Radio-Variability

We present VLA 8.5 GHz lightcurves of the two quasar images in the gravitational lens B1600 + 434, obtained from a monitoring campaign between February 1998 and September 2002. The lightcurves were produced using 4 seasons of ∼8 months in which the two images are well separated. Thanks to a strong peak in the intrinsic flux of the lensed quasar in the last season, we have been able to obtain the most precise and robust time delay of this system to date: $\Delta t = 40.1 \pm 1.2$ (random) ± 1.0 (systematic) days (4.8% precision at the 68% confidence level). We also report the detection of short-term extrinsic variability ($\sim 3-4$ times larger than what is expected from the 1.1% measurement errors), which occurs at the $3-5$% level on time scales of $\sim$ days/weeks. In addition, we have detected variations in the flux-ratio of the lensed images from season to season (6% from the beginning to the end of the ~ 4 years monitoring campaign), which are indicative of extrinsic variability in longer time-scales (≥ 7 months). The observed extrinsic variability can be caused by two physical mechanisms: scintillation/scattering in the lens galaxy or the Milky Way, or microlensing of a superluminal jet-component in the quasar due to massive compact objects in the lens galaxy. A detailed analysis in the context of these two physical models will be done in a forthcoming publication.

A. Berciano Alba, L.V.E. Koopmans, C. D. Fassnacht & A. G. de Bruyn, in prep.

2.1 Introduction

Multiply imaged quasars constitute unique astrophysical systems, since they can be used as cosmological probes, as well as laboratories to study both the lens and source structure. The fundamental parameter involved in these kind of studies is the *time delay*, that is, the difference between the propagation times of two images[1], which depends on the cosmology, the projected lens potential and the quasar and lens redshifts.

On the cosmological side, time delays offer the prospect of determining the Hubble parameter (H_0) without the need to rely on local distance indicators (Refsdal 1964), a topic that has being the main driver of time delay measurements since the discovery of the first lens (Walsh et al. 1979). For individual lenses, this method can provide H_0 estimates with an error better than 10% if, together with a well constraint mass model of the lens, the time delay measurement errors are of the order of $3\% - 5\%$. From the 19 time delay lenses known to date, 10 reach this level of precision (see Table 2.1). In addition, there is a weaker dependence between the time delay and the other cosmological parameters (the matter density of the Universe Ω_m, the dark energy density Ω_{de}, the curvature Ω_k, and the dark energy equation of state parameters w_0 and w_a) which is usually ignored. However, given the dramatic increase on the known time delay lenses expected from the forthcoming optical and radio surveys, the ability of time delays to constrain other cosmological parameters is also starting to be explored (Mörtsell & Sunesson 2006; Dobke et al. 2009; Coe & Moustakas 2009). Finally, time delays can also be used to constrain the slope of the lensing density profile [2] by adopting the value of H_0 obtained by other methods[3]. In addition, Keeton & Moustakas (2009) have recently proposed a new formalism to use time delays as a proxy for Dark Matter substructures in lens galaxies.

Measurements of time delays require intensive monitoring campaigns aimed to produce well sampled lightcurves for the individual lensed images. These lightcurves can show two kinds of variability: (i) correlated *intrinsic* variability, due to physical processes that are taking place in the quasar and (ii) uncorrelated *extrinsic* variability, due to effects produced by structures in our galaxy or in the lens galaxy that happen to be lying along the line-of-sight of each image. When the same intrinsic fluctuations are observed in two lightcurves, they can be cross correlated to derive the time delay and flux-ratio between the corresponding images. Once these two parameters are known, they can be used to calculate the ratio between the lightcurves of two lensed images (flux ratio lightcurve hereafter) in order to isolate the extrinsic variability. If this extrinsic component is negligible, the lightcurves can be combined to improve the sampling of the intrinsic fluctuations observed in the quasar and compare them with models of AGN structure (e.g., Kawaguchi et al. 1998; Goicoechea et al. 2008). Otherwise, the flux ratio lightcurve can provide valuable information about the compact objects in the lens galaxy and the structure of the source (and/or the intervening ionized medium, if the lens is observed in the radio) .

[1] since the ray path lengths differ for each observed image, their associated absolute light travel times are also different.

[2] the baryon-dark matter transition region of the lens galaxy where multiple images are usually found.

[3] e.g., $H_0 = 72 \pm 8$ km s^{-1} Mpc^{-1} from the HST Key Project (Freedman et al. 2001).

Table 2.1: *Current gravitational lens systems with measured times delays. Refrences between parentheses correspond to papers that have only been published in astro-ph.*

Lens Name	band	images	time delay	accuracy (%)	references
B0218+357	8.4, 15 GHz	AB	10.5 ± 0.4	3.8	Biggs et al. (1999)
B1422+231	8.4, 15 GHz	AB	1.5 ± 1.4	93.3	Patnaik & Narasimha (2001)
		AC	7.6 ± 2.5	32.9	
		BC	8.2 ± 2.0	24.4	
B1600+434	8.5 GHz	AB	$47.0^{+12.0}_{-9.0}$	25.5	Koopmans et al. (2000)
	I-band	AB	51.0 ± 4.0	7.8	Burud et al. (2000)
B1608+656	8.5 GHz	AB	$31.5^{+2.0}_{-1.0}$	6.3	Fassnacht et al. (2002)
	8.5 GHz	BC	36.0 ± 1.5	4.2	
		BD	$77.0^{+2.0}_{-1.0}$	2.6	
PKS 1830-211	8.4, 15 GHz	AB	44.0 ± 9.0	20.5	van Ommen et al. (1995)
	8.6 GHz	AB	$26.0^{+4.0}_{-5.0}$	19.2	Lovell et al. (1998)
		AB	$24.0^{+5.0}_{-4.0}$	20.8	(Wiklind & Combes 1999)
HE 0435-1223	R-band	AD	$-14.4^{+0.8}_{-0.9}$	6.3	Kochanek et al. (2006)
		AB	$-8.0^{+0.7}_{-0.8}$	10.0	
		AC	$-2.1^{+0.8}_{-0.7}$	38.1	
HE 1104-1805	R-band		161.0 ± 7.0	4.3	Ofek & Maoz (2003)
	A,B-band		157.0 ± 21.0	13.4	Wyrzykowski et al. (2003)
	R-, B-band		$152.2^{+2.8}_{-3.0}$	2.0	Poindexter et al. (2007)
HE 2149-2745	V-, I-band	AB	103.0 ± 12.0	11.7	Burud et al. (2002a)
RX J0911+0551	I-band	A1B	143.0 ± 6.0	4.2	Hjorth et al. (2002)
		A2B	149.0 ± 8.0	5.4	
		A3B	154.0 ± 16.0	10.4	
RX J1131-1231	R-band	AB	$12.0^{+1.5}_{-1.3}$	12.5	(Morgan et al. 2006)
		AC	$9.6^{+2.0}_{-1.6}$	20.8	
		AD	-87.0 ± 8.0	9.2	
SBS 0909+532	R-band	BA	$-45.0^{+1.0}_{-11.0}$	24.4	Ullán et al. (2006)
	R-band		-49.0 ± 6.0	12.2	Goicoechea et al. (2008)
SBS 1520+530	R-band	AB	130.0 ± 3.0	2.3	Burud et al. (2002b)
	V-, R-band		130.0 ± 3.0	2.3	Gaynullina et al. (2005)
Q0957+561		AB	417.0 ± 3.0	0.7	Kundic et al. (1997)
Q2237+0305	R-band	BA	-6.0 ± 41.0 h		Vakulik et al. (2006)
		CA	35.0 h		
		DA	2.0 ± 44.0 h		
	X-rays	AB	$2.7^{+0.5}_{-0.9}$ h	33.3	Dai et al. (2003)
SDSS J1004+4112	R-band	BA	40.6 ± 1.8	4.4	Fohlmeister et al. (2008)
		CA	821.6 ± 2.1	0.3	
SDSS J1650+4251	R-band	AB	49.5 ± 1.9	3.8	Vuissoz et al. (2007)
FBQ 0951+2635	R-band	AB	16.0 ± 2.0	12.5	Jakobsson et al. (2005)
PG 1115+080	V-band	BC	23.7 ± 3.4	14.3	Schechter et al. (1997)
		BC	$25.0^{+3.3}_{-3.8}$	15.2	Barkana (1997)
	X-rays	AB	$2.7^{+0.5}_{-0.9}$	33.3	Dai et al. (2001)
WFI J2033-4723	R-band	BA	35.5 ± 1.4	3.9	Vuissoz et al. (2008)
		BC	$62.6^{+4.1}_{-2.3}$	6.5	

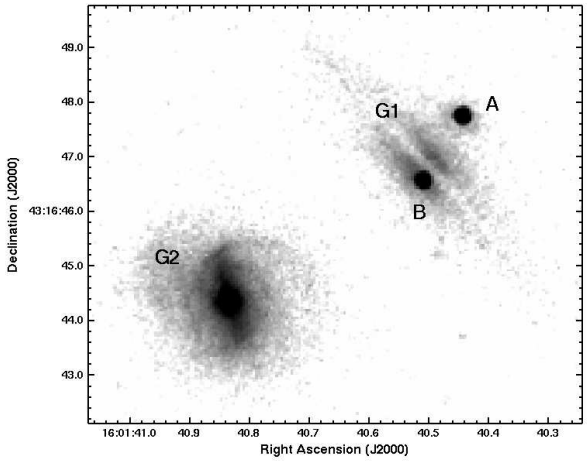

Figure 2.1: *HST/WFPC2 image of the lens system B1600+434 obtained with the F814W filter (HST GO Program 8268, PI Impey), courtesy of M. Auger. The labels indicate the main lens galaxy G1 (an edge-on late type spiral with a prominent dust lane), its companion G2 (a face-on barred spiral) and the quasar images A and B.*

The gravitational lens B1600 + 434 (B1600 hereafter) is a doubly imaged quasar that was discovered in the CLASS[4] radio survey by Jackson et al. (1995) (see Fig. 2.1). The main lens galaxy (G1) is an edge-on late-type spiral with a nearby companion (G2) which is a nearly face-on barred spiral (Jaunsen & Hjorth 1997; Koopmans et al. 1998). Both galaxies lie in a group of at least seven late-type galaxies at $z \sim 0.41$, with a velocity dispersion of 90 km s^{-1} (Auger et al. 2007). The two images A and B, separated by $1.39 \pm 0.01''$, correspond to a background quasar located at redshift $z = 1.589 \pm 0.006$ (Fassnacht & Cohen 1998). The ray path of image A passes mainly through the dark matter halo of G1, whereas the ray path of image B passes predominantly through its disk and bulge. The time delay between both images has been estimated to be 47^{+12}_{-9} days from VLA[5] 8.5 GHz radio observations (26% precision at the 95% confidence level; Koopmans et al. 2000, K00 hereafter) and 51 ± 4 days from optical observations (8% precision at the 95% confidence level; Burud et al. 2000), with image A leading.

The radio observations of K00, carried out over a period of 8 months (February - October 1998), showed the presence of an intrinsic decrease in the flux density of both lensed images, plus short term extrinsic variability (time scales from days to weeks) which appears to be much stronger in image A than in image B. Interestingly, this is the only time delay radio lens (out of the 5 with measured time delays to date) that has shown this kind of variability. Two plausible explanations have being suggested: (i) a combination of scattering in the lensing galaxy and scintillation caused by the ionized component of the interstellar medium (ISM) in our own galaxy, or (ii) radio

[4]Cosmic Lens All-sky Survey (Myers et al. 2003; Browne et al. 2003).
[5]Very Large Array, located in New Mexico.

microlensing by massive compact objects in the lens galaxy.

Unlike in the case of optical microlensing (e.g., Paraficz et al. 2006), there is still no conclusive proof of the detection of microlensing in the radio domain. The reason is that, since the typical sizes of compact radio sources[6] are much larger than the typical separation between the caustics in the magnification pattern (few μas), all the possible microlensing variability is smoothed out and therefore very difficult to observe (Wambsganss 1990). However, if the quasar has a relativistic jet-component moving towards the observer, Doppler boosting could make mJy sources observed at high frequencies look small enough to make radio microlensing detectable (e.g., Gopal-Krishna & Subramanian 1991, K00 also describes this in detail).

Using WSRT[7] observations at 1.4 GHz and 5 GHz and the VLA 8.5 GHz observations form K00, Koopmans & de Bruyn (2000) (KdB00 hereafter) analyzed the frequency dependence of the extrinsic variability observed in B1600 and concluded that the microlensing scenario (in which a superluminal jet-component in the quasar is being microlensed by compact objects in the halo of the lens galaxy) is a preferred alternative over scintillation. However, high-resolution (0.5 mas) VLBA[8] observations at 15 GHz have failed to detect the core-jet structure in the quasar images (Patnaik & Kemball 2001). Moreover, these data suggest that image B is scatter-broadened at the lens, so that its size is larger than that of image A, and hence could scintillate less than image A.

The possibility that the extrinsic variability of B1600 might be due to microlensing is very exciting, since it would provide a tool to constraint the mass function of compact objects in the dark-matter halo of G1, as well as information about the structure of the possible quasar radio jet (KdB00). To see whether this mechanism is indeed the dominant cause of the observed variability in image A, a multi-wavelength observational campaign was carried out with the VLA between June 1999 and January 2003 to monitor this system. This Chapter focuses on the analysis of the high-resolution 8.5 GHz observations of this campaign (in which both lensed images are well separated) combined with the 8.5 GHz observations presented in K00. Since radio sources often show stronger and faster brightness variations at high-frequencies, these observations are expected to provide the best time delay estimate of the whole multi-wavelength campaign. Therefore, the immediate goals in this Chapter are (i) to provide an improved time-delay measurement of B1600 and (ii) use this delay to investigate the presence of extrinsic variability, as found in K00.

The outline of this Chapter is as follows. In Sect. 2 we present the relevant information about the full VLA observational campaign. In Sect 3, we describe the data reduction procedure adopted for the 8.5 GHz observations. The resultant lightcurves of the B1600 lensed images are presented in Sect. 4, together with the corresponding error analysis. Section 5 describes the method used to calculate the time delay and flux ratios and the results derived from it. The characterization of the extrinsic variability present in the lightcurves is discussed in Sect. 6. Summary and conclusions are presented in Sect. 7.

[6] ≥ 1 mas for ≥ 1 Jy flat spectrum sources at low frequencies, and several tens of μas for ~ 10 mJy sources at high frequencies.

[7] Westerbork Synthesis Radio Telescope, located in The Netherlands.

[8] Very Long Baseline Array.

Table 2.2: *Information about the full VLA monitoring campaign. Season 1 correspond to the observations used in Koopmans et al. (2000) and Koopmans & de Bruyn (2000). Observations and array configurations that were not used in this work are indicated between parenthesis.*

Season	Project	Start date	End date	Array config.	Epochs	Bands
1	AX004	13/02/1998	09/06/1998	A, AB	52	X
1	AF340	11/06/1998	19/10/1998	AB, B	40	X
2	AB922	15/06/1999	12/02/2000	(AD), A, AB, B	92	L, C, X
	(AK507)	19/02/2000	20/06/2000	(BC), (C), (CD)	41	X, U, K
3	AK518	06/10/2000	29/05/2001	(D), A, AB, B	67	L, C, X, U
4	AK543	17/01/2002	28/09/2002	(D), A, AB, B, (BC)	80	L, C, X, U
	(AK554)	01/10/2002	05/01/2003	(BC), (C)	32	C, X, U

VLA observing bands: K=22 GHz, U=15 GHz, X=8.5 GHz, C=5.0 GHz, L=1.4 GHz

Table 2.3: *Average integration time per epoch during the X-band observations for the phase calibrator (J1549+506), the flux calibrator (B1634+627) and the lens (B1600+434). The minimum and maximum integration time used in each project are indicated between parenthesis. The names of the projects that were not used in this work are also indicated between parentheses.*

Project	J1549 + 506 Int. time (min)	B1634 + 627 Int. time (min)	B1600 + 434 Int. time (min)
AX004	7 (2.0 - 13)	6 (1.2 - 8.8)	9 (5.0 - 10)
AF340	3 (1.0 - 5.8)	6 (2.3 - 11)	11 (4.0 - 20)
AB922	3 (1.2 - 5.7)	2 (0.7 - 4.9)	4 (2.2 - 9.5)
(AK507)	2 (1.4 - 3.8)	1 (0.4 - 1.6)	4 (2.2 - 6.6)
AK518	2 (1.7 - 4.3)	1 (0.6 - 1.2)	5 (3.1 - 8.4)
AK543	2 (1.3 - 2.7)	1 (0.6 - 1.2)	5 (1.2 - 10)
(AK554)	2 (1.6 - 2.2)	1 (0.8 - 1.2)	12 (9.7 - 22)

2.2 Observations

The lens B1600 was monitored with the VLA in continuum mode[9] from February 1998 to January 2003 as part of a multi-source campaign. The details of these observations are summarized in Table 2.2. Note that the full campaign includes observations in several bands and VLA configurations. The results presented here correspond to the analysis of the 8.5 GHz (X-band) data[10], since it is the highest frequency which has being observed during the full 4 year observing period. In addition, we focused in the A, BnA, and B configuration data because these are the only ones that provide enough angular resolution at this frequency to resolve the lensed images (between 0.2″ and 0.7″). The typical observing time per epoch spent in the phase calibrator (J1549 + 506), the flux calibrator (B1634 + 627, also known as 3C343), and the lens are listed in Table 2.3. The average time interval between epochs is 3.3 days.

Figure 2.2 shows a map of the phase calibrator, the flux calibrator and the lens,

[9] two IFs of 50 MHz, each containing right and left circular polarizations and one channel.
[10] IFs centered at 8.4351 GHz and 8.4851 GHz.

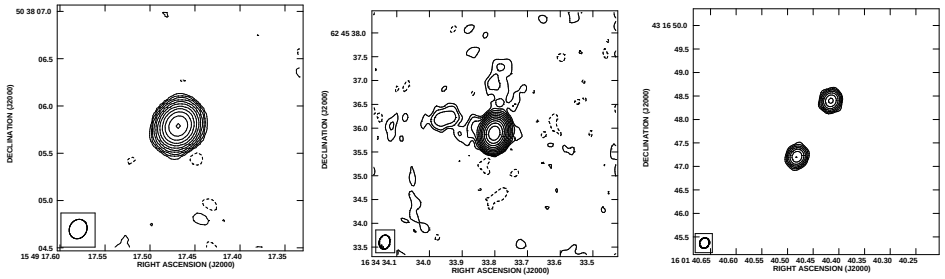

Figure 2.2: *VLA 8.5 GHz maps of the observed sources, produced using one of the A-array epochs.* ***Left panel:*** *J*1549 + 506*, the phase calibrator. Contours are drawn at -2, 2, 4, 8, 16, 32, 64, 128, 256, 512, 1024 and 2048 times the* 4.6×10^{-4} *Jy noise level.* ***Central panel:*** *B*1634 + 627 *(3C343), the flux calibrator. Contours are drawn at -2, 2, 4, 8, 16, 32, 64, 128, 256, 512, 1024 and 2048 times the* 2.0×10^{-4} *Jy noise level.* ***Right panel:*** *the lensed images. Contours are drawn at -4, 4, 8, 16, 32, 64, 128 and 256 times the* 9.0×10^{-5} *Jy noise level.*

produced using the data of one of the A configuration epochs. J1549 + 506 is a compact, flat spectrum source, so its intrinsic flux is expected to vary significantly withing time scales of the order of months. B1634 + 627, on the other hand, is an extended steep spectrum source (not expected to be variable on these time scales) which is resolved by the VLA in A configuration. These sources are detected with signal-to-noise ratios (SNR) of the order of $\sim 100 - 1000$.

2.3 Data Reduction

The data reduction was conducted using the NRAO[11] data reduction package AIPS, following the same calibration procedure adopted in K00. Instead of using the flux calibrator (B1634 hereafter) to establish the absolute flux scale of the observations, we set an approximate flux scale by assigning a constant flux of 1 Jy to the phase calibrator (J1549 hereafter). Since J1549 is a variable source, the difference between its real flux and the arbitrary flux scale can change considerably during the 4 year observing period. Therefore, by using the phase and gain solutions derived with J1549 as first-order calibration for the B1634 and B1600 data, we are transferring the intrinsic variability of J1549 to the B1634 and B1600 lightcurves. Since the flux of B1634 is considered to be constant, dividing the lightcurves of the lensed images by the lightcurve of B1634 should remove all of the J1549 variability and calibration errors from them. The absolute flux scale is recovered by dividing the B1634 lightcurve by the true flux of the source (normalized B1634 lightcurve hereafter), for which a value of 0.84 ± 0.01 Jy[12] is adopted.

To facilitate the data reduction process and make it uniform for all epochs, this procedure was implemented in a semi-automatic pipeline written in *Parseltongue*

[11] National Radio Astronomy Observatory.
[12] based on WSRT 8.5 GHz observations carried out in December 1998, see K00.

(Python interface to classic AIPS, see Kettenis et al. 2006). The different steps followed for the data reduction of each source are described in the following sections.

2.3.1 Phase Calibrator

After setting the flux of J1549 to 1 Jy with SETJY, the first and last 10 seconds of each scan of J1549, B1634 and B1600 are removed with QUACK. Then, the average flux and rms of the J1549 data are estimated with FINDR, to clip potential outliers with fluxes 20σ above the average.

Using a point-like source model, preliminary amplitude and phase solutions are derived with CALIB for time intervals of the average observing scan. A second run of FINDR and CLIP is carried out to remove outliers with flux-deviations larger than 5σ above the average, after which the data of each IF and polarization are manually inspected and flagged with TVFLG and WIPER. Finally, the bandpass shape is calibrated, and the final amplitude and phase solutions are re-calculated by running CALIB for a second time. To assess the quality of the final calibration, we create a contour map of J1549, and graphs of the visibility amplitudes as function of time and UV distance. If corrupted data were still present, TVFLG and WIPER would be run again and the final calibration repeated.

2.3.2 Flux Calibrator

After proper interpolation, the final amplitude and phase solutions obtained with the phase calibrator are applied to the B1634 and B1600 data. As in the previous case, outliers are removed by setting a clipping level of 20σ before the data of each IF and polarization are manually inspected and flagged with TVFLG and WIPER. A contour map of B1634, together with plots of the visibility amplitudes as function of time and UV distance, are made to verify that all corrupted data were removed.

Once the data have being satisfactory edited, the first-order phase solutions are further refined through an iterative cycle of cleaning (which provides a new clean component model of B1634 in each iteration) and phase-only self-calibration. The full cycle is composed by seven iterations in which the depth of the cleaning is gradually increased and the time interval for which the phase solutions are derived is gradually decreased. When the full cycle is completed, the resultant contour map and visibility plots are inspected again in case that more corrupted data shows up. If these plots are considered to be satisfactory, the flux of B1634 is obtained by summing the flux of all the clean components of the final model, which is then divided by 0.84 Jy to express it in terms of a normalized flux scale.

For the cleaning step of the iterative cycle, we create one set of clean boxes[13] that contain the low surface brightness features shown in Fig. 2.2. This set of boxes was used in the data reduction of all epochs. Therefore, for those epochs in which these faint features are not detected or not resolved, we could be introducing spurious clean components in the final model of B1634 that will affect the derived flux. However, since this source is detected with SNR~100, the effect of spurious clean components is expected to be negligible.

[13] areas of the B1634 dirty map in which the clean algorithm is allowed to look for clean components

Table 2.4: *Parameters used to characterize the two Gaussian components in the initial X-band B1600+434 model, taken from 8.5 GHz VLBA observations (Koopmans et al. 2000). The coordinates are given respect to the phase center (*RA = 16^h 1^m 40.446^s, DEC = 43° 16′ 47.76″*).*

Lensed image	Δ RA (arcsec)	Δ DEC (arcsec)	Flux (mJy beam^{-1})	diameter (mas)
A	-0.333	0.6368	30.1	1
B	0.3902	-0.5529	23.4	1

Nonetheless, we decided to get an alternative estimate of the B1634 flux in each epoch as consistency check. In order to do that, we produced tapered maps for each epoch by limiting the UV-range such as to provide a clean beam with the major axes between 3.5″ and 2.5″ (so B1634 is "seen" by the interferometer as an unresolved source). The task UVFIT was then used to fit a Gaussian model to the data within the specified region of the UV-plane (note that the calibration still corresponds to the phase and gain solutions derived using all the baselines). The flux of B1634 is obtained from the best Gaussian fit. As a result, two lightcurves of B1634 were produced: one using the fluxes derived with the clean component models, and the other one using the fluxes derived from the tapered data. The resultant lightcurve ratio has an rms scatter of ∼ 0.52% arround a mean value of 0.42%, which indicates that the fluxes derived from the clean-component model are systematically higher than the ones derived from the tapered data. This is probably due to the fact that the Gaussian fit in the UV-plane is not perfect, resulting in an under-estimation of the flux obtained from the tapered data.

2.3.3 Lensed Images

The data reduction procedure followed for the B1600 data is identical to the one described for B1634, with the exception of the iterative cleaning and phase self-calibration cycle, which is replaced by an iterative model fitting and phase self-calibration cycle.

Given that the lensed images are unresolved in the A-array configuration maps, the system is modeled with two Gaussians which parameters have been set according to higher resolution VLBA 8.5 GHz observations (K00, see Table 2.4). After refining the first-order phase solutions by re-calibrating the data with this initial model, the task UVFIT is used to update the model by fitting two Gaussians in the UV-plane. Since the size and positions of the lensed images in the initial model are well constrained from the VLBA observations, only the flux of the Gaussians is optimized. The updated model is used to improve the calibration of the data, and the process is iterated 4 times. The resulting flux of each lensed image corresponds to the peak flux of the Gaussian components in the final model.

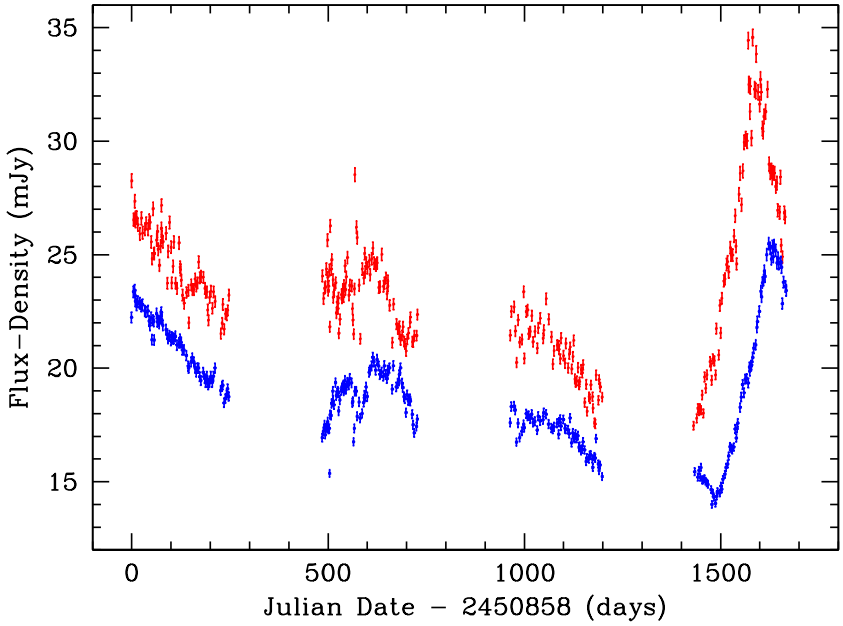

Figure 2.3: *Normalized VLA 8.5 GHz lightcurves of the B1600+434 lensed images A (red) and B (blue) between 13/02/1998 (2450858) and 08/09/2002. The error bars indicate the final* 1.1% *measurement error estimated for each data point (see Sect. 2.4.1 for details).*

2.4 Lightcurves

Once the full data reduction was completed, the resulting maps of B1634 and B1600 were inspected to identify obvious problematic epochs. In this way, we noticed 20 epochs of B1634 and 8 epochs of B1600 that showed strong artifacts in the final maps. The overlap between the epochs associated with both sets of maps was only 2. A posterior inspection of the lightcurves also revealed the presence of 2 outliers in the second season of the B1634 lightcurve, and two outliers in the B1600 lightcurve (one in season 1, which epoch was already identified as problematic when inspecting the B1634 maps, and the other one in season 2). All these epochs were removed from the final lightcurves.

2.4.1 Error analysis

The errors associated with each point of the B1634 and B1600 lightcurves can be divided in two main categories: (i) systematic, which affect all the epochs in the same way (resulting in an absolute flux scale error), and (ii) random, which affect each epoch independently. Since, as it will be shown in Sect. 2.5 and 2.6, both the determination of the time delay and the characterization of extrinsic variability

involve the ratio of the two lensed image lightcurves, any source of systematic error will have no impact in the results derived for these two quantities. The random error, on the other hand, can have three different origins: (i) residual RFI[14] errors, due to imperfect data flagging and incomplete UV coverage, (ii) noise errors, given by the rms noise of each source map in each epoch, and (iii) amplitude and phase calibration errors.

Calibration errors can be caused by, for example, pointing inaccuracies and atmospheric conditions, but also by the way in which the sources are modeled during the self-calibration procedure. This is particularly relevant in the case of B1634, due to its complicated extended structure (see Fig. 2.2). In K00, both the flagging and the self-calibration of B1634 and B1600 were carried out with the DIFMAP package (only the calibration of J1549 was done in AIPS). In particular, they used a single Gaussian component to first model fit the visibilities of B1634, after which the Gaussian fitting was replaced by image cleaning to include the extended structure in the final model. Since we have edited and self-calibrated the data presented in K00 in a different and independent way[15], the residual RFI and calibration errors can be estimated by comparing the results provided by both methods.

The ratio between the first season of the B1634 and B1600 lightcurves presented here, and the ones presented in K00, show an rms scatter of $\sim 1\%$. This corresponds to a systematic error for each lightcurve point of $1/\sqrt{2} = 0.72\%$. On the other hand, the average thermal noise error per epoch is about 0.4 mJy beam^{-1} for B1634 and 0.09 mJy beam^{-1} for the lensed images (0.04% and 0.4% respectively). As a result, the total measurement error assumed for each point of the final B1600 lightcurve is: $\sqrt{0.42^2 + 2 \times 0.72^2} \sim 1.1\%$. The factor 2 accounts for the calibration errors in B1634, because the final B1600 lightcurve is divided by the lightcurve of B1634.

2.4.2 Structure of the lightcurves

The final normalized lightcurves of the B1600 lensed images[16] are shown in Fig. 2.3. The long-term flux changes ($\sim$ months) are probably due to intrinsic variability of the quasar, whereas the short term fluctuations ($\sim$ days/weeks) can have both an intrinsic and/or extrinsic origin.

The most prominent feature corresponds to the steep increase of the flux in the last 8 month season of the lightcurve (a factor ~ 2 between the minimum and the maximum), after which the flux of both images start to decrease again. From the relative position of this flux peak in the two lightcurves it is clear that image B lags image A in time, in agreement with the predictions of the lens model presented in Koopmans et al. (1998). As it will be shown in Sect. 2.5, this feature will allow us to obtain a more precise estimate of the time delay than the ones that are currently available.

[14] Radio Frequency Interference.

[15] Note that, for the self-calibration of the B1600 data, K00 used the same initial model adopted here (see Table 2.4). However, the solution intervals and number of iterations were different than the ones implemented in our pipeline, which in general will make both procedures converge in a different way (so they can be treated as independent).

[16] B1600 lightcurves divided by the B1634 normalized lightcurve.

The most remarkable feature, however, corresponds to the dramatic flux increase (and posterior decrease) of image A on a time scale of several weeks in the second season. Since this feature is not present in the in the lightcurve of image B, it must have an extrinsic origin. A more detailed description of this event will be presented in Sect. 2.6.

2.5 Time delay and flux ratio

To estimate the time delay and flux ratio between the lensed images, we use the *minimum-dispersion method* developed by Pelt et al. (1996). The idea of this method is to find the time and flux corrections (Δt and f) that have to be applied to lightcurve B in order to find the best match with lightcurve A. This is carried out by means of the composite lightcurve C, which contains the data points of lightcurve A and the corrected data points of lightcurve B. A generic point on the composite lightcurve is described as:

$$C_n(t_n) = \begin{cases} A_i & \text{if } t_n = t_i \\ fB_j & \text{if } t_n = t_j + \Delta t \end{cases}$$

Given a particular value of Δt and f, the dispersion of this composite lightcurve is a measure of the goodness of the match between the lightcurves A and B. Therefore, the true time delay and flux ratio between the lensed images correspond to the values of Δt and f that minimize the rms dispersion of lightcurve C inside a sliding window function.

The dispersion measure used in our calculations indicates how close two points C_n and C_m are in the composite lightcurve. It is given by:

$$D_4^2(\Delta t, f) = \frac{\sum_{n=1}^{N-1} \sum_{m=n+1}^{N} S_{m,n} W_{m,n} G_{m,n} (C_n - C_m)^2}{\sum_{m=n+1}^{N} S_{m,n} W_{m,n} G_{m,n}} \tag{2.1}$$

Note that this dispersion function includes not only strictly neighboring pairs, to get a statistically more stable curve by adding more $(C_n - C_m)^2$ points. The variable $G_{m,n}$ guarantees that the dispersion is measured in the overlap areas of the lightcurves A and B ($G_{m,n} = 1$ when C_n and C_m are from different lightcurves, and $G_{m,n} = 0$ otherwise). The variable $W_{n,m}$ weights the pairs taking into account the 1σ error of their flux densities (σ_i):

$$W_{m,n} = \frac{W_n W_m}{W_n + W_m}; \quad W_i = \frac{1}{\sigma_i^2} \tag{2.2}$$

Finally, $S_{m,n}$ is the decorrelation weight function, which is introduced to avoid correlation between two points separated by a long time gap[17]. The form of $S_{m,n}$ adopted in this work is :

$$S_{m,n} = \exp\left(\frac{-(\mathrm{t_m} - \mathrm{t_n})^2}{2\tau^2}\right) \tag{2.3}$$

[17]note that, since the noise observed in quasar lightcurves is random, long time correlation is not expected to happen.

where τ is the decorrelation time scale in days.

The error associated with the time delay and the flux ratio derived with this method was estimated following a Monte-Carlo (MC) approach. In order to do that, a sample of 1000 A and B lightcurve pairs was generated by changing the noise values of each data point. Since the true underlying lightcurves are unknown, we doubled the variance of the MC lightcurves by adding, to the measurement error of each data point, a random noise value which is extracted from a Gaussian distribution with σ equal to the measurement error (1.1%). The minimum of the dispersion function associated with each lightcurve pair was determined by exploring the parameter space for Δt between 0 and 100 days, and f between 1.1 and 1.4 . In this way, a time-delay and a flux ratio probability distribution function (PDF) were generated from the values of Δt and f obtained for each lightcurve pair in our MC sample (see Fig. 2.4). The time-delay and flux ratio of each season derived from the PDFs (which were computed for three different decorrelation time scales) are listed in Tables 2.5 and 2.6, respectively. Note that doubling the variance of the noise on the observed lightcurves leads to a conservative error estimate on the time-delay.

Figure 2.5 shows the minimum of the dispersion function associated with the observed lightcurves independently calculated for each season. Note that the most precise and least degenerate estimate of the time delay comes from season 4, as a consequence of the good sampling of the flux peak present in this part of the lightcurve. If we compare the time delays derived from the other seasons with this one ($\Delta t_i/\Delta t_4$, see Table 2.5), we see that the differences between them are consistent within the errors. However, a similar comparison between the corresponding flux ratios (ϕ_i/ϕ_4, see Table 2.6) shows discrepancies of $3-4\sigma$ ($2-3\%$) between season 1 and season 4 (also between season 2 and season 4), and $7-8\sigma$ ($5-6\%$) between season 1 and season 4. In other words, the flux ratio between the lensed images changes during the ~4 year monitoring campaign, which indicates the presence of extrinsic variability on time scales of ≥ 7 months.

Because of this significant variation in the flux ratio (which can clearly be seen in Fig. 2.5), using the data from all the seasons simultaneously to calculate the time delay yields a biased result. Instead, the final time delay obtained for each decorrelation time scale τ (see *Full* in Table 2.5) is calculated by weighting the values derived independently for each season:

$$\Delta t_{Full} = \frac{\sum \Delta t_i/\sigma_i^2}{\sum 1/\sigma_i^2} \pm \left(\sum 1/\sigma_i^2\right)^{-1/2} \tag{2.4}$$

A small decorrelation time scale is very sensitive to the short term variability in the lightcurves (more pronounced in A than in B), whereas a large decorrelation time is more sensitive to their long term gradients. Therefore, we consider that $\tau = 6$ days gives the best estimate of the time delay and the flux ratios, although the estimated time-delays change by < 1 days for these different assumptions. Therefore, to be in the conservative side, we add ± 1 day of systematic error to the rms value, to take into account the effect of the decorrelation time scale. In this way, the final best estimate for the time delay becomes: Δt = 40.1 ± 1.2 (random) ± 1.0 (systematic) days (4.8% precision at the 68% confidence level, from the weighted average for $\tau = 6$).

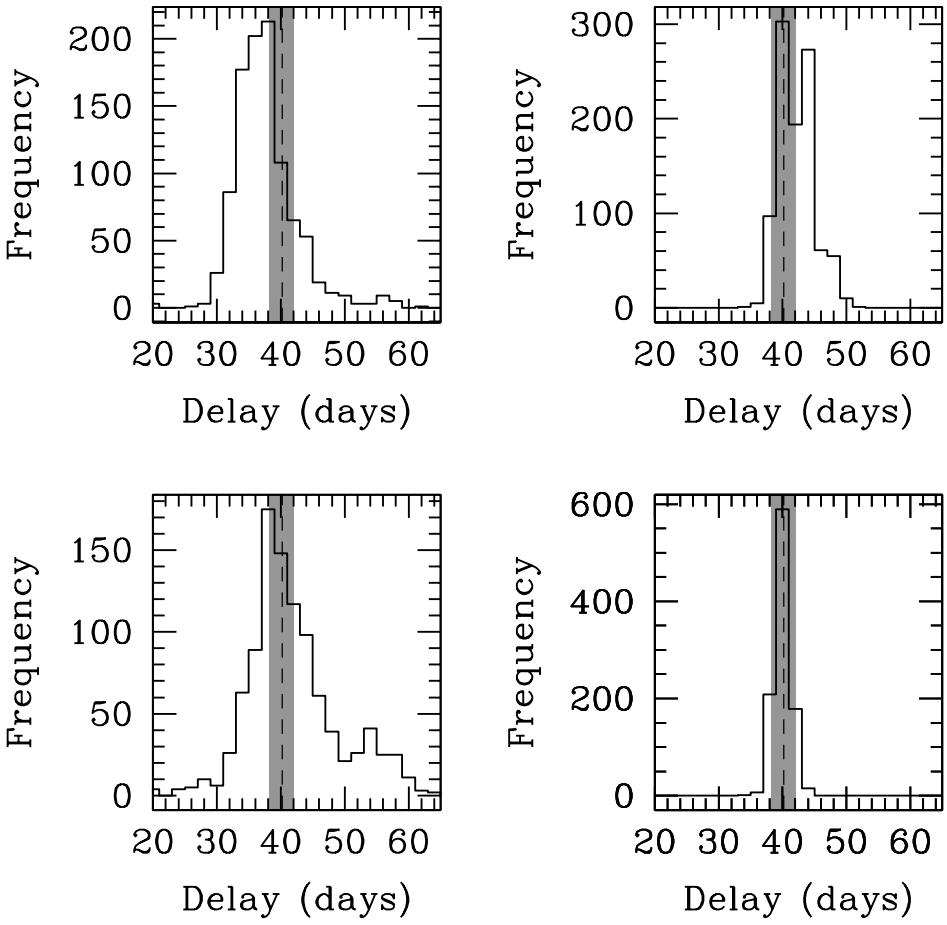

Figure 2.4: *Time delay probability distribution functions (PDFs) obtained when the minimum dispersion method is combined with Monte Carlo simulations using a decorrelation time scale of τ = 6 days. The dashed line indicated the best estimate of the time delay, whereas the shaded region indicates its uncertainty (Δt_{Full} = 40 ± 1.9 days for τ =6, see the end of Sect. 2.5 for details). The different panels correspond to season 1 (top left), season 2 (top right), season 3 (bottom left) and season 4 (bottom right).*

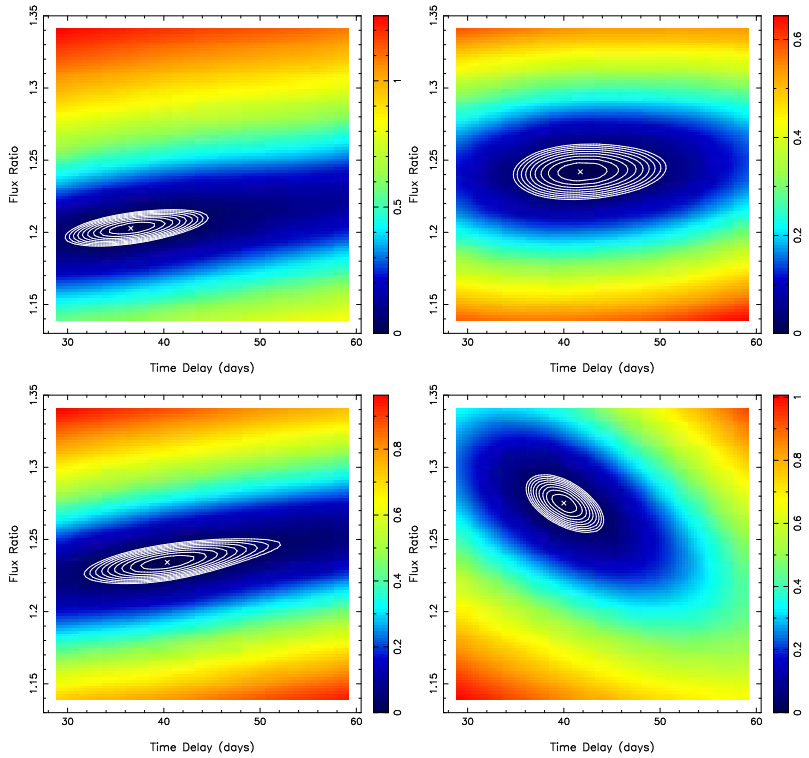

Figure 2.5: *Minimum of the dispersion function associated with the observed lightcurves of the lensed images (*1.1% *measurement error), independently calculated for each season. The different panels correspond to season 1 (top left), season 2 (top right), season 3 (bottom left) and season 4 (bottom right). The white contours (which purpose is to illustrate the behavior of the dispersion and the degeneracies between delay and flux-ratio) are spaced by a factor of 1.01. Note that both the colors and contours are plotted in logarithmic scale.*

The time delays obtained in this work for season 1 are shorter and better constrained than the ones reported in K00 (see Table 2.7), despite the fact that both were determined following the same method. The reason is that K00 fixed the flux ratio to 1.212 ± 0.005, whereas we consider it as a free parameter. As a graphical illustration of this point, let's consider the upper left panel of Fig. 2.5. Note that the region of the dispersion function minimum (indicated with white ellipses) is rather flat and nearly horizontal. Therefore, a small increase in the flux ratio results into a rapid increase in the time delay uncertainty. Since the flux-ratio that we currently find is lower than the assumed value on K00, both the time delay and its associated uncertainty are reduced.

On the other hand, our new time delay is inconsistent at the 3σ level with the value of 51 days obtained from optical observations (Burud et al. 2000). In fact, as can be seen in Fig. 2.4, the peak of the time delay PDF of each observing season is close to 40 days, whereas 51 days always lies in the region of lowest probability.

Table 2.5: *Time delays (Δt) derived from each season using three different decorrelation time scales (τ). The Δt values correspond to the mean and rms of the time delay probability distribution function (PDF) obtained when the minimum dispersion method is combined with Monte Carlo simulations (see Sect. 2.5 for details). The values between parentheses correspond to the median and the 68% confidence level (84% minus 16% quartile divided by two) of the PDF. The columns Δ_{ti}/Δ_{t4} list the ratio between the mean time delay of each season and season 4, where the errors have been derived following standard propagation techniques. The ratio obtained using the median values is indicated between parentheses. The raw labeled* Full *lists the weighted average of the time delays from all epochs derived with Eq. (2.4). The best estimate of the time delay corresponds to the weighted average for $\tau = 6$ including an extra ± 1 day error due to systematics (see Sect. 2.5 for details).*

	$\tau = 3$ days		$\tau = 6$ days		$\tau = 12$ days	
Season	Δt (days)	$\Delta t_i/\Delta t_4$	Δt (days)	$\Delta t_i/\Delta t_4$	Δt (days)	$\Delta t_i/\Delta t_4$
1	40.9 ± 6.1 (41.2 ± 6.4)	1.0 ± 0.2 (1.0 ± 0.2)	37.7 ± 5.7 (37.0 ± 3.8)	0.9 ± 0.1 (0.9 ± 0.1)	37.1 ± 8.6 (38.0 ± 4.8)	0.9 ± 0.2 (0.9 ± 0.1)
2	43.1 ± 5.5 (42.2 ± 6.5)	1.1 ± 0.1 (1.0 ± 0.2)	42.1 ± 2.7 (41.7 ± 2.7)	1.1 ± 0.1 (1.0 ± 0.1)	43.4 ± 1.8 (43.4 ± 1.6)	1.1 ± 0.1 (1.1 ± 0.1)
3	43.0 ± 5.1 (43.8 ± 4.5)	1.1 ± 0.1 (1.1 ± 0.1)	41.9 ± 7.2 (40.7 ± 6.4)	1.0 ± 0.2 (1.0 ± 0.2)	42.6 ± 8.6 (42.0 ± 6.5)	1.1 ± 0.2 (1.0 ± 0.2)
4	40.7 ± 2.1 (40.7 ± 2.2)	–	40.1 ± 1.3 (40.1 ± 1.3)	–	40.6 ± 1.1 (40.5 ± 1.0)	–
Full	41.2 ± 3.1 (41.4 ± 3.3)	–	40.4 ± 1.6 (40.1 ± 1.6)	–	41.4 ± 1.3 (41.2 ± 1.1)	–

Table 2.6: *Flux ratios derived from each season using three different decorrelation time scales (τ). The values correspond to the mean and rms of the flux ratio probability distribution function (PDF) obtained when the the minimum dispersion method is combined with Monte Carlo simulations (see Sect. 2.5 for details). The median and the 68% confidence level (84% minus 16% quartille divided by two) give the same results. The columns ϕ_i/ϕ_4 list the ratio between the mean flux ratio of each season and season 4, where the errors have been derived following standard propagation techniques. The significance of the flux ratio changes from season to season (signif.) is calculated as $(1 - \phi_i/\phi_4)/\mathrm{error}_{\phi_i/\phi_4}$. The best estimates correspond to $\tau = 6$.*

	$\tau = 3$ days			$\tau = 6$ days			$\tau = 12$ days		
Season	Flux ratio	ϕ_i/ϕ_4	signif.	Flux ratio	ϕ_i/ϕ_4	signif.	Flux ratio	ϕ_i/ϕ_4	signif.
1	1.206 ± 0.007	0.947 ± 0.008	6.7	1.203 ± 0.007	0.944 ± 0.007	8.2	1.202 ± 0.009	0.946 ± 0.008	6.5
2	1.242 ± 0.005	0.975 ± 0.007	3.5	1.241 ± 0.005	0.974 ± 0.006	4.4	1.242 ± 0.005	0.978 ± 0.006	3.9
3	1.236 ± 0.008	0.971 ± 0.008	3.4	1.235 ± 0.009	0.969 ± 0.008	3.8	1.235 ± 0.010	0.972 ± 0.009	3.1
4	1.273 ± 0.008	–	–	1.274 ± 0.006	–	–	1.270 ± 0.006	–	–

Table 2.7: *Comparison between the time delays presented in Koopmans et al. (2000), and the ones derived in this work using the same data (season 1, see Table 2.2). The columns show: decorrelation time scale (τ), previous estimates of the time delay (Δt_{B-A}), time delays obtained in this work (Δt) and flux ratios obtained in this work (Flux ratio). Note that, in Koopmans et al. (2000), the flux ratio was fixed to* 1.212 ± 0.005 *days.*

τ (days)	Δt_{B-A} (days)	Δt (days)	Flux ratio
3	46^{+7}_{-8}	40.88 ± 0.36	1.2055 ± 0.0007
6	46^{+6}_{-5}	37.70 ± 0.51	1.2031 ± 0.0007
12	48^{+5}_{-6}	39.70 ± 0.66	1.2045 ± 0.0009

Table 2.8: *Flux ratios derived by Fassnacht et al. (2002) for the three pairs of images observed in the lens system B*1608 + 656. *The columns ϕ_i/ϕ_1 list the ratio between the flux ratio of each season and season 1, where the errors have been derived following standard propagation techniques. The significance of the flux ratio changes from season to season (signif.) is calculated as* $(1 - \phi_i/\phi_1)/\mathrm{error}_{\phi_i/\phi_1}$.

Image pair	Season	Flux ratio	ϕ_i/ϕ_1	signif.
AB	1	2.042 ± 0.012	–	–
AB	2	1.986 ± 0.014	0.973 ± 0.009	3.1
AB	3	2.006 ± 0.014	0.982 ± 0.009	2.0
CB	1	1.039 ± 0.006	–	–
CB	2	1.031 ± 0.007	0.992 ± 0.009	0.9
CB	3	1.028 ± 0.007	0.989 ± 0.009	1.2
DB	1	0.351 ± 0.002	–	–
DB	2	0.345 ± 0.003	0.983 ± 0.010	1.7
DB	3	0.342 ± 0.003	0.974 ± 0.010	2.5

Therefore, given the agreement between the independent time delays obtained for each of the four observing seasons (which are also better sampled than the optical lightcurves), we conclude that the new lower estimate is more appropriate. Note also that the optical flux ratio derived by Burud et al. (2000) is $A/B = 1.50$, whereas our best estimate for the first season is $A/B = 1.203 \pm 0.007$.

Finally, it is worth mentioning that there is another lens in which long term flux ratio changes have being observed: the four-image system B1608 + 656 (Fassnacht et al. 2002). However, the significance of the flux ratio changes from season to season is lower than in B1600+434 (see Tables 2.6 and 2.8).

2.6 Extrinsic variability

Figure 2.6 shows a blowup of each season of the B1600 lightcurves, before and after the time delay and flux ratios have being taken into account. From the comparison between the green and red lightcurves it is clear that image A shows more scatter than image B on time scales of ~days / weeks, a feature that is not only present in season 1 (as already reported in K00) but also in the other three seasons. Note that, as shown in Fig. 2.7 and Table 2.9, the fluctuations in season 4 only appear to be smaller because of the difference in flux-density scale.

This short term variability can have three causes: (i) calibration errors, (ii) intrinsic variability in the quasar, and (iii) extrinsic variability due to structures (e.g., small-scale ISM or potential fluctuations) in our galaxy or in the lens galaxy that happen to be lying along the line of sight.

Since the intrinsic quasar variability is the same in both images, the extrinsic component can be isolated by dividing the lightcurve of image B by the lightcurve of image A. For this, lightcurve B has to be corrected for the time delay and scaled to match lightcurve A using the corresponding flux ratios. Finally, lightcurve B is interpolated to the times of the lightcurve A data points, and the resulting interpolated B lightcurve is divided by the A lightcurve. Note that, because image B hardly varies on short time-scales, interpolating its flux-densities leads to negligible errors in comparison to interpolating the lightcurves of image A.

Figure 2.7 shows the resultant flux ratio lightcurve split in the individual seasons. The dotted lines correspond to the average measurement error, which is clearly smaller than the fluctuations present in all the seasons. In order to characterize the significance of the the observed short-term variability we use the modulation index:

$$\mathrm{MI} = \sqrt{\frac{\mathrm{rms}^2 - \sigma^2_{\mathrm{aver}}}{\sigma^2_{\mathrm{aver}}}} \tag{2.5}$$

The resultant MI values obtained for each season show that these fluctuations are $\sim 3-4$ times larger than what is expected from the estimated measurement errors (see Table 2.9). This result constitutes a robust indication of the extrinsic nature of most of the observed short-term variability, which is predominantly taking place in the lightcurve of image A. Moreover, the second season of the flux ratio lightcurve shows flux density fluctuations of $\sim$ 15% between 29/08/1999 and 24/09/1999 with MI~7 (S2 event, see Table 2.9). If we look at the top right panel of Fig. 2.6, we see that in this period (561.5 and 592.25 days) the lightcurve of image A experiences a strong sharp variation in the observed flux-density that is clearly not observed in lightcurve B.

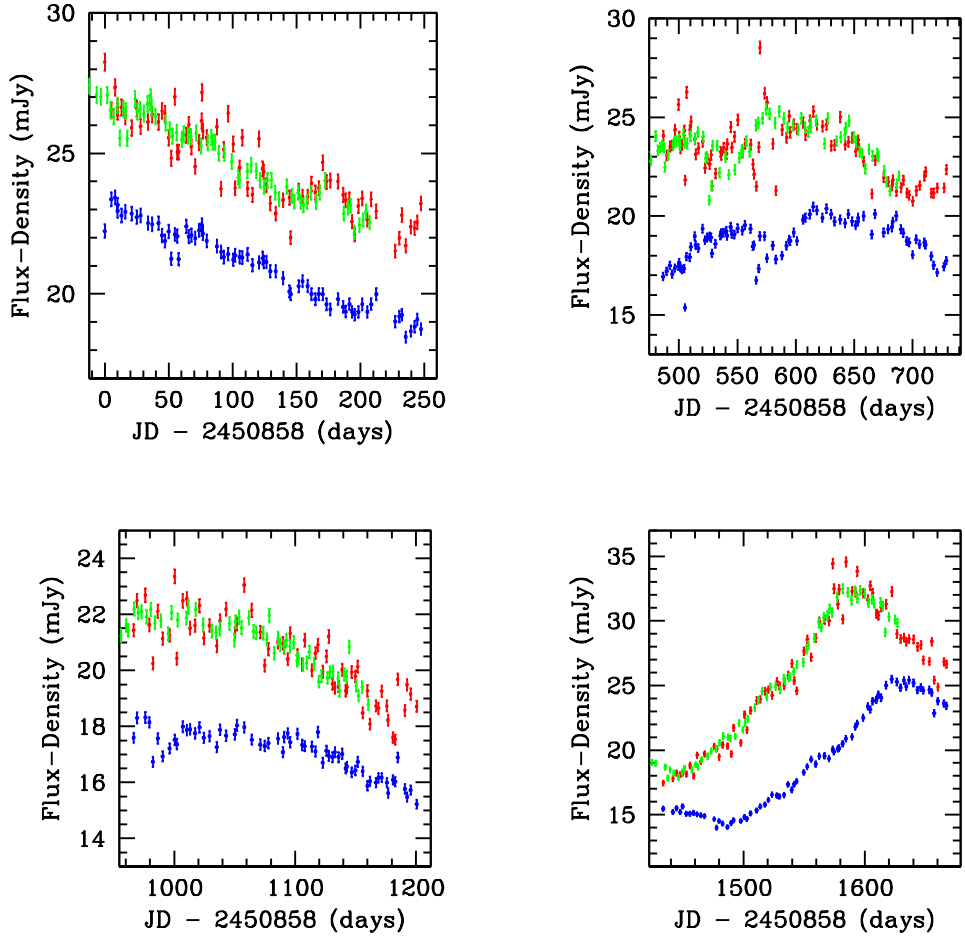

Figure 2.6: *Blowup of each season in the normalized lightcurves of the B1600+434 lensed images presented in Fig. 2.3. The green points correspond to the lightcurve of image B, after being corrected using a time delay of* $\Delta t = 40$ *days and the flux ratios listed in Table 2.6 for* $\tau = 6$*. The different panels correspond to season 1 (top left), season 2 (top right) season 3 (bottom left) and season 4 (bottom right).*

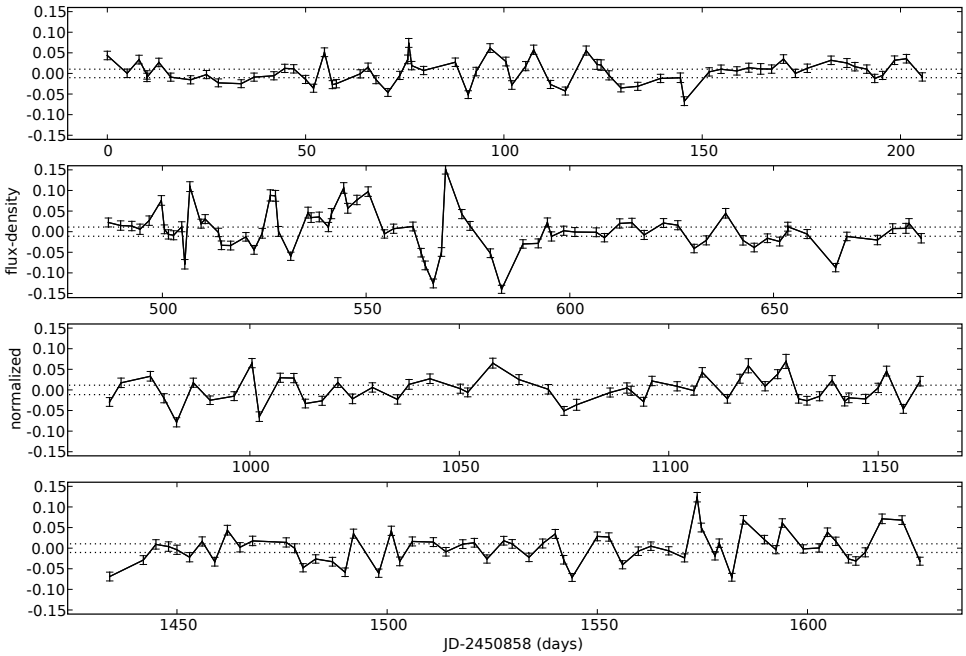

Figure 2.7: *Ratio of the A and B image lightcurves after correcting for both the time delay (Δ = 40 days) and the flux density ratio of each season obtained for τ = 6 (see Table 2.6). The dotted lines indicate the region in which the variability would be expected if it was only due to measurement errors (see Table 2.9). Panels from top to bottom correspond to season 1, 2, 3 and 4.*

Table 2.9: *Characterization of the extrinsic variability observed in the flux ratio lightcurves displayed in Fig. 2.7. The columns show: lightcurve segment (season), rms scatter (rms), average measurement error ($\sigma_{\rm aver}$) and modulation index (MI, see Eq. 2.5). Errors have been derived following standard propagation techniques.*

Season	rms (%)	$\sigma_{\rm aver}$ (%)	MI
1	2.8 ± 0.007	1.0	2.57 ± 0.76
2	4.9 ± 0.013	1.1	4.31 ± 1.19
3	3.3 ± 0.011	1.1	2.67 ± 1.04
4	3.8 ± 0.010	1.1	3.44 ± 1.02
S2 event	8.0 ± 0.050	1.1	7.43 ± 4.70

2.7 Summary and Conclusions

The gravitational lens B1600+434 is a doubly imaged quasar for which the time delay had previously been measured both in optical (51±4 days, Burud et al. 2000) and radio (47^{+12}_{-9} days at 8.5 GHz, Koopmans et al. 2000). What makes this system extremely interesting is the presence of short term extrinsic variability in the radio lightcurve of image A (Koopmans et al. 2000), which could be due to microlensing by compact objects in the halo of the main lens galaxy (G1, see Fig. 2.1) or scattering/scintillation by the ISM in G1 or/and in our own galaxy.

To identify which of these two mechanisms is the dominant cause of the observed extrinsic variability, a multi-wavelength observational campaign was carried out with the VLA between June 1999 and January 2003 to monitor this system. This Chapter focuses on the analysis of the 8.5 GHz high resolution observations of this campaign (in which both lensed images are well separated), including the observations between February 1998 and October 1988 presented in Koopmans et al. (2000) (4 seasons of ∼ 8 months in total). The main results of this analysis can be summarized as follows:

- Thanks to the good sampling of an intrinsic flux peak present in the last season of the A and B lightcurves, we have obtained the most precise and robust time delay estimate of this system to date: $\Delta t = 40.1 \pm 1.2$ (random) ± 1.0 (systematic) days (4.8% precision at the 68% confidence level). The method used to derive this value was the one proposed by Pelt et al. (1996) (minimum dispersion method), combined with Monte-Carlo simulations to estimate the errors involved. Whereas this new time-delay is consistent with the one derived in K00, it differs at the 3σ level respect to the optical time-delay presented in Burud et al. (2000). This suggests that the errors estimated for the optical time delay have been underestimated.

- We report the detection of significant short-term extrinsic variability in each of the four seasons of the image A lightcurve (∼ 3 – 4 times larger than what is expected from the 1.1% measurement errors), which happens at the 3 – 5% level on time scales of ∼ days/weeks.

- The data also show variations in the flux-ratio of the lensed images from season to season (6% from the beginning to the end of the ∼ 4 years monitoring campaign), which are indicative of extrinsic variability on time-scales of ∼ 7 months.